SUPPLEMENTAL INFORMATION

Carbon photochemistry: Towards a Solar Reverse Boudouard Refinery.

Camilo J. Viasus Pérez[1,2,*], Juan Manuel Restrepo-Florez[3], Jessica Ye[1], Nhat Truong Nguyen[4], Athanasios A. Tountas[1], Rui Song[1], Chengliang Mao[1], Andrew Wang[1], Abdelaziz Gouda[1], Samantha Corapi[1], Shufang Ji[1], Hamish MacLeod[1], Jiaze Wu[1], Alán Aspuru-Guzik[1,7], Christos T. Maravelias[5,6], and Geoffrey A. Ozin[1*†].

[1] *Department of Chemistry, University of Toronto, Toronto, Ontario, Canada, ON, M5S 3H6.*

[2] *Grupo de Investigación en Química de Coordinación y Bioinorgánica, Departamento de Química, Facultad de Ciencias, Av. Carrera 30 # 45-03, Universidad Nacional de Colombia – Sede Bogotá, Colombia.*

[3] *Department of Chemical and Biological Engineering, University of Wisconsin-Madison, 1415 Engineering Dr, Madison, WI 53706*

[4] *Department of Chemical and Material Engineering, Gina Cody School of Engineering and Computer Science, Concordia University, 1455 De Maisonneuve Blvd W, Montreal, Quebec H3G 1M8, Canada*

[5] *Department of Chemical and Biological Engineering, Princeton University, 50-70 Olden St, Princeton, NJ 08540, USA.*

[6] *Andlinger Center For Energy and the Environment, 86 Olden St, Princeton, NJ 08540, USA.*

[7] *Department of Computer Science, University of Toronto, Sandford Fleming Building, 10 King's College Road, Toronto, ON M5S 3G4*

[†] *Lead Contact*

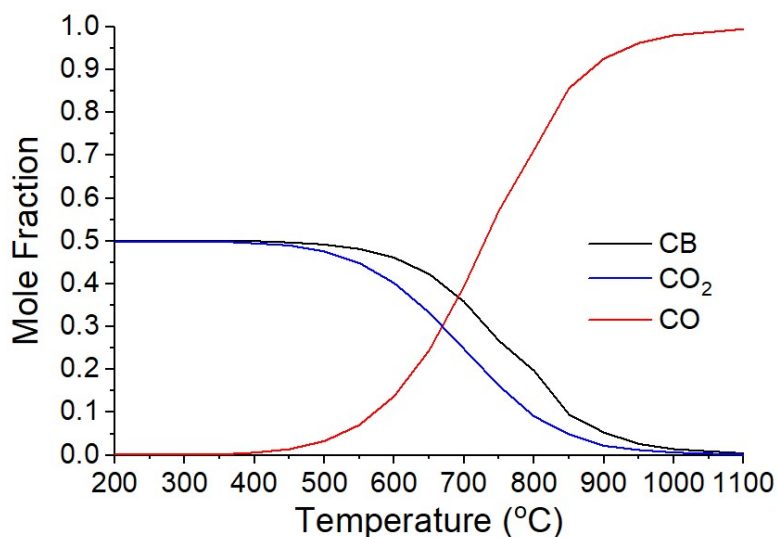**Correspondence: g.ozin@utoronto.ca, cjviasusp@gmail.com*

Figure S1. Thermal equilibrium simulation for the reverse Boudouard reaction (Factsage software following the C + CO_2 → 2CO reaction molar ratio at 1 atm of pressure). The selected temperature range was from 200 to 1100 °C at intervals of 50°C.
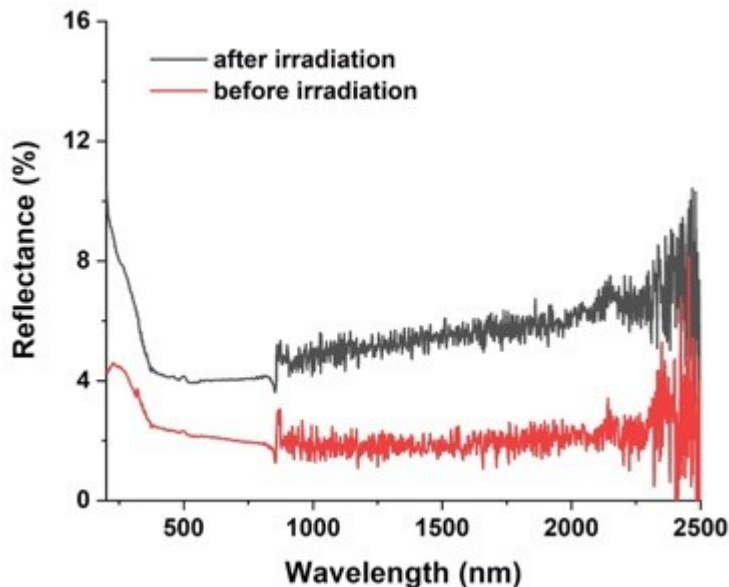
Figure S2. UV-vis spectrum of CB before and after light irradiation confirms carbonaceous materials' high light absorption. Samples were shown to be stable with no apparent modifications detectable by optical methods following light irradiation under reverse Boudouard conditions.

Since the UV vis spectrum of the used carbon samples showed very low reflectance properties (~2 % average in the full range from 300 to 2500nm), it is safe to assume that most light irradiation used in the natural solar and solar simulated experiments were absorbed and could contribute in chemical and thermally induce reverse Boudouard.
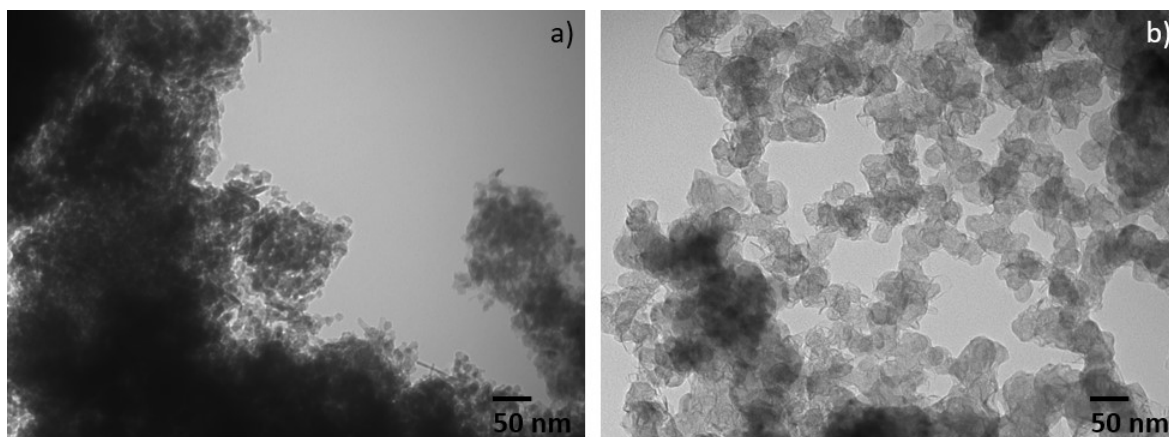

Figure S2a. TEM of a) Biochar and b) Alfaaesar carbon

Table S2-1. ICP-MS of CB CABOT sample of 0.4116 g. The total amount of the primary metals is 169.4 ppm and is distributed as in the following table.

Metal	ppm	Metal	ppm	Metal	ppm	Metal	ppm	Metal	ppm
Be	0.18	Pb	0.36	V	1.09	Fe	4.62	Si	9.84
Ag	0.18	Cr	0.49	Ti	1.46	Mg	5.59	Sb	11.18
Cu	0.24	Ni	0.67	Ba	1.82	K	6.01	Mo	11.48
Mn	0.30	Zn	0.91	As	2.31	Al	7.96	Ca	26.18
Co	0.30	Tl	0.91	Se	2.55	B	8.26	Na	64.57

Table S2-2. XPS % concentration of the assigned binding energy functionaly found.

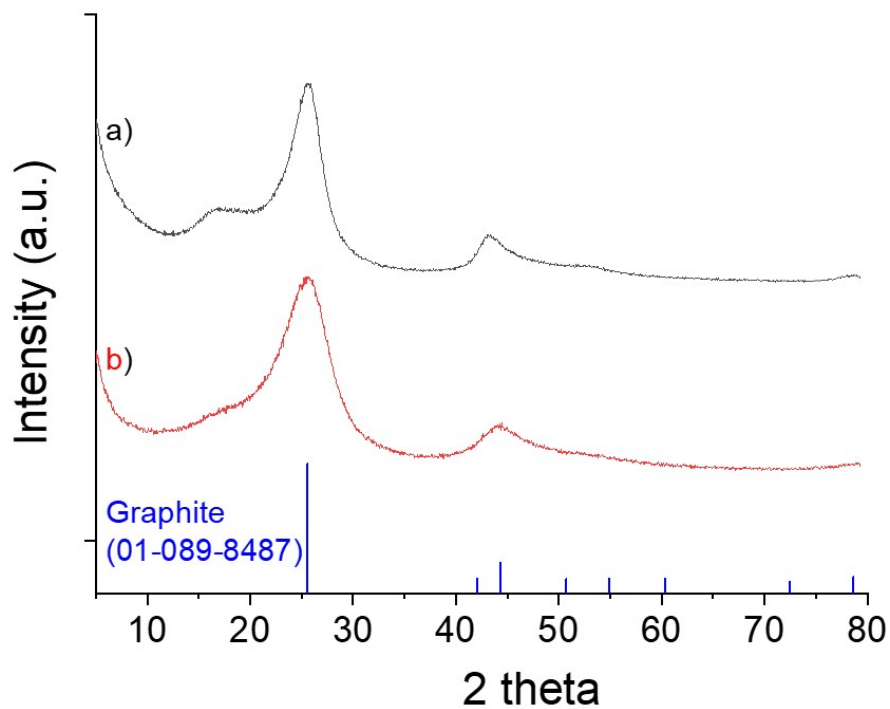| Assigned bond	% conc. Before CO_2 and light	% conc. After CO_2 and light
O-C=O	3.86	6.26
C-O	8.03	5.42
C-C	44.02	59.37
C=C	44.09	28.95

Figure S3. XRD pattern of [12]CB (CABOT) material before (b) and after (a) photo-driven Boudouard. Carbon samples showed two main broad signals implying low graphitic structure with slightly asymmetric displacement on the crystalline plane 100 (44.5 2Θ) and preserved the diffraction 002 planes at 26.6 2Θ after light irradiation. This behaviour suggests that the structure is resilient to photodegradation during CO production. These results agree with published data [1].
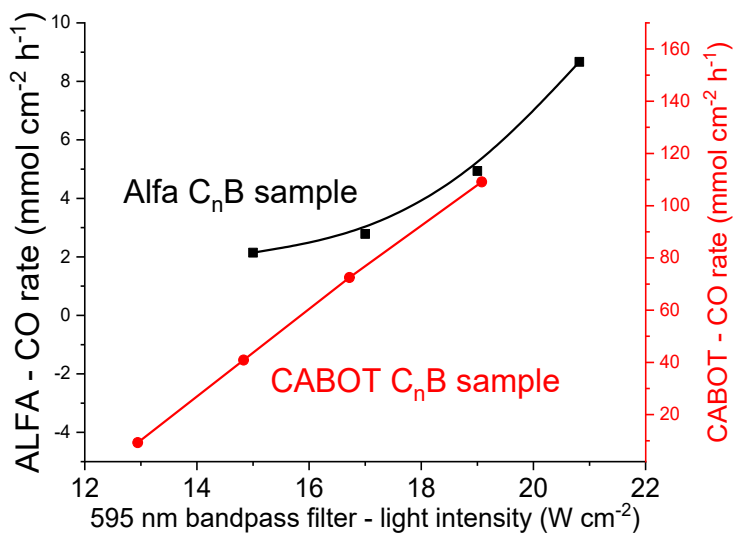
Figure S4. Photo-driven Boudouard reaction using a 595 nm filter in CABOT C_nB and ultrapure C_nB (Alfa C_nB) samples. At a light intensity lower than 21 W cm^{-2} and a reactor temperature of 350 °C, the ultrapure C_nB sample presented Arrhenius behaviour while the CABOT sample exhibited a linear trend characteristic of photochemical behaviour. In addition, a higher CO rate was observed in the CABOT sample at the same conditions.

Material S5

Procedure for kinetic experiments, Figure S5: Xe arc lamp light intensity was set to 34 W cm^{-2} and the reactor pressure was set to 29.7 psig in each run. The sample was weighed before and after the batch reaction step times shown in **Figure 2f**. Hydrogen, carbon monoxide and methane concentration were quantified using a GC instrument (SRI8610) calibrated using calibration standards for H_2 (250, 500 and 1000 ppm), CO (198, 523 and 5000 ppm) and CH_4 (261, 523 and 5000 ppm). CH_4 was omitted in the graph due to the shallow concentration produced (< 0.005%). The reactivity of the photo-driven reverse Boudouard process was evaluated using the time expression represented in equation e1.

$$t = Ao \int_{fA1}^{fA2} \frac{d fA}{(rA)SA}$$

(e1)

Where Ao is the initial CO_2 moles, rA is the reaction rate, SA is the exposed surface area to light, and fA_1 and $fA2$ are the fractions of reactants over time (CO_2 concentration remaining).

From the first-rate law

$$rA = k\,A$$

(e2)

Where k is the reaction constant and A is the CO_2 moles over time. Graphically, we could determine the reaction order n for the photo-driven reverse Boudouard reaction, as shown in (e3).

$$\ln (rA) = \ln k + n\ln (A)$$

(e3)

From e2, we could replace A as the mol fraction expression and

$$fA = \frac{Ao - A}{Ao}$$

(e4)

to produce (e5)

$$rA = k\,(Ao)(1 - fA)$$

(e5)

Once we replace (e5) in (e1) and integrate over the reaction fraction fA_1 and $fA2$ we can obtain the reaction constant k for each reaction time as presented in (e6)

$$k = \frac{1}{SA.t}(-\ln (1 - fA))$$

(e6)

As a result, $k = 0.0367 \pm 0.00258$ h^{-1} was calculated from each step time and stoichiometry of the reaction produced 2x rA which represents CO rate, is calculated as 0.886 $\pm\,0.064$ mmol cm^{-2} h^{-1}.

Experimental data collected during the kinetic experiments

Time (minutes)	ppm CO produced	C_nB mass (mg) over time	ppm H2 produced	% CO2 conversion
0.5	12885±4500	192.3±0.05	914±80.2	0.21
1	25328±5263	192.2±0.06	1564±151	0.42
2	46231±6011	191.7±0.07	1708±201	0.77
3	77504±4650	190.8±0.10	1343±111	1.28
4	85186±15111	189.6±0.25	2265±351	1.41
5	120189±7211	188.1±0.06	2388±299	1.99

An additional reverse photo-driven Boudouard experiments were performed for an extended time (10, 20 and 30 minutes) and generated a maximum CO_2 conversion of 2.59, 2.89 and 6.59 % respectively. Xe arc lamp light intensity was set to 28.4 W cm^{-2} and the reactor pressure was set in average to 15.5 psig in each run. The system was not presenting an equilibrium state after this period. A prominent conversion of CO_2 also suggests de feasibility of using natural solar light (higher intensities) for industrial applications.
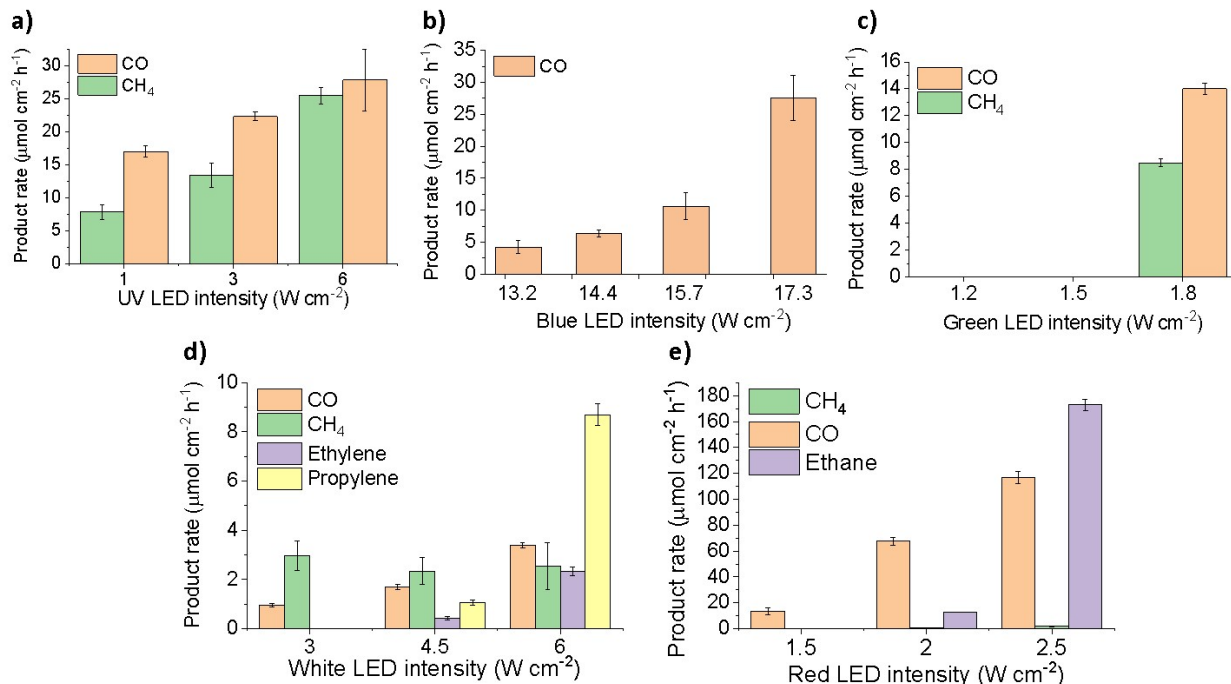
Figure S6. LED wavelength dependence tests on reverse Boudouard using CABOT C_nB. Conditions: 15–20 psi of CO_2, 60 minutes irradiation, UV LED at 365 nm. b) Wavelength dependence tests using blue LED at 470 nm. c) wavelength dependence using green LED at 525 nm. d) Wavelength dependence tests using white LED between 420–600 nm and e) wavelength dependence using 625 nm red LED.
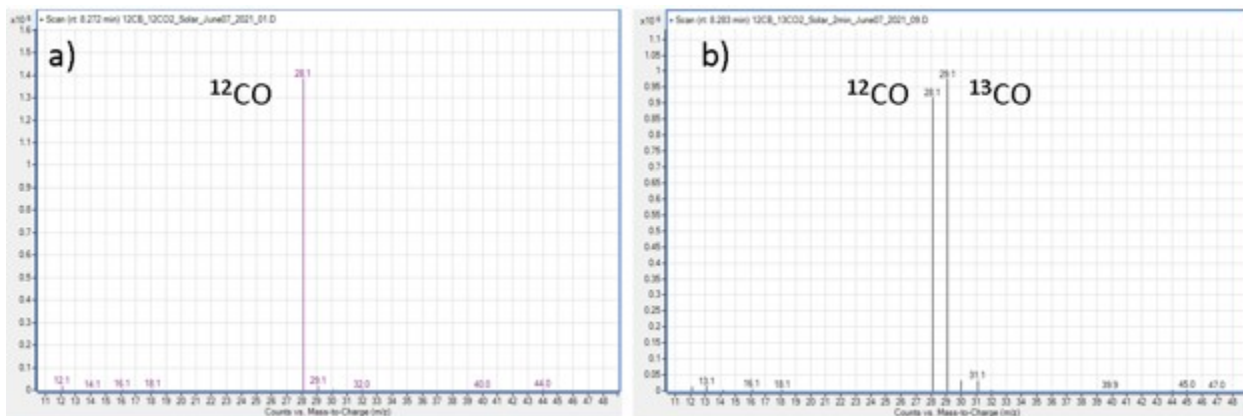

Figure S7. Isotopic distribution for reverse Boudouard solar test using $^{12}CB + ^{12}CO_2$ (a) and $^{12}CB + ^{13}CO_2$(b). An almost equal $^{12}CO/^{13}CO$ isotopic ratio distribution confirms that CO_2 provides equivalent carbon contribution as C_nB in the formation of CO product. Relative intensities and normalized values for the isotopic experiments using $^{12}CO_2$ and $^{13}CO_2$ over carbon black.

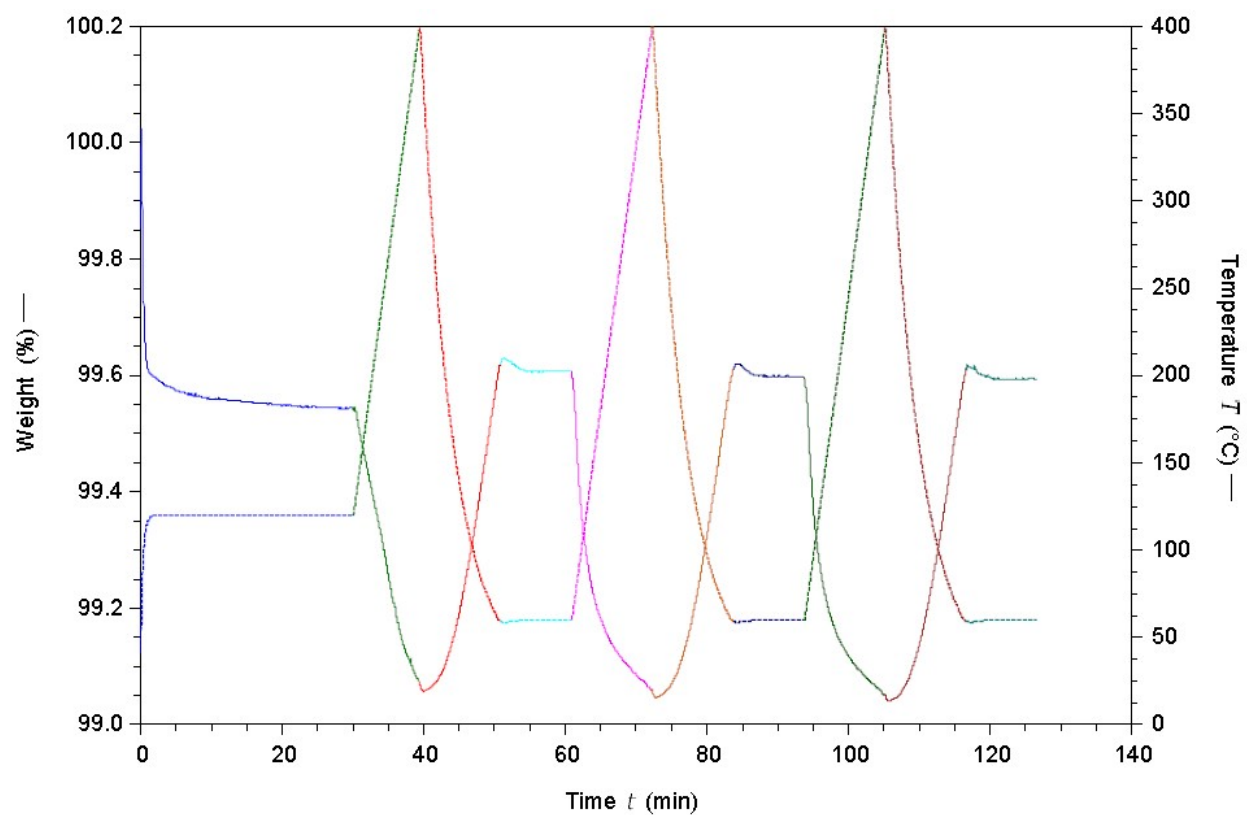| Isotope products/Conditions	$^{12}C_nB + ^{12}CO_2$ Normalized intensity	$^{12}C_nB + ^{13}CO_2$ Normalized intensity
^{12}CO	945	465
^{13}CO	55	535

Figure S8. TGA uptake experiments of CO_2 over CABOT C_nB sample. An average CO_2 absorption of 125.3 ± 3.4 mmol CO_2 / gC_nB (0.57 % w CO_2/w C_nB).
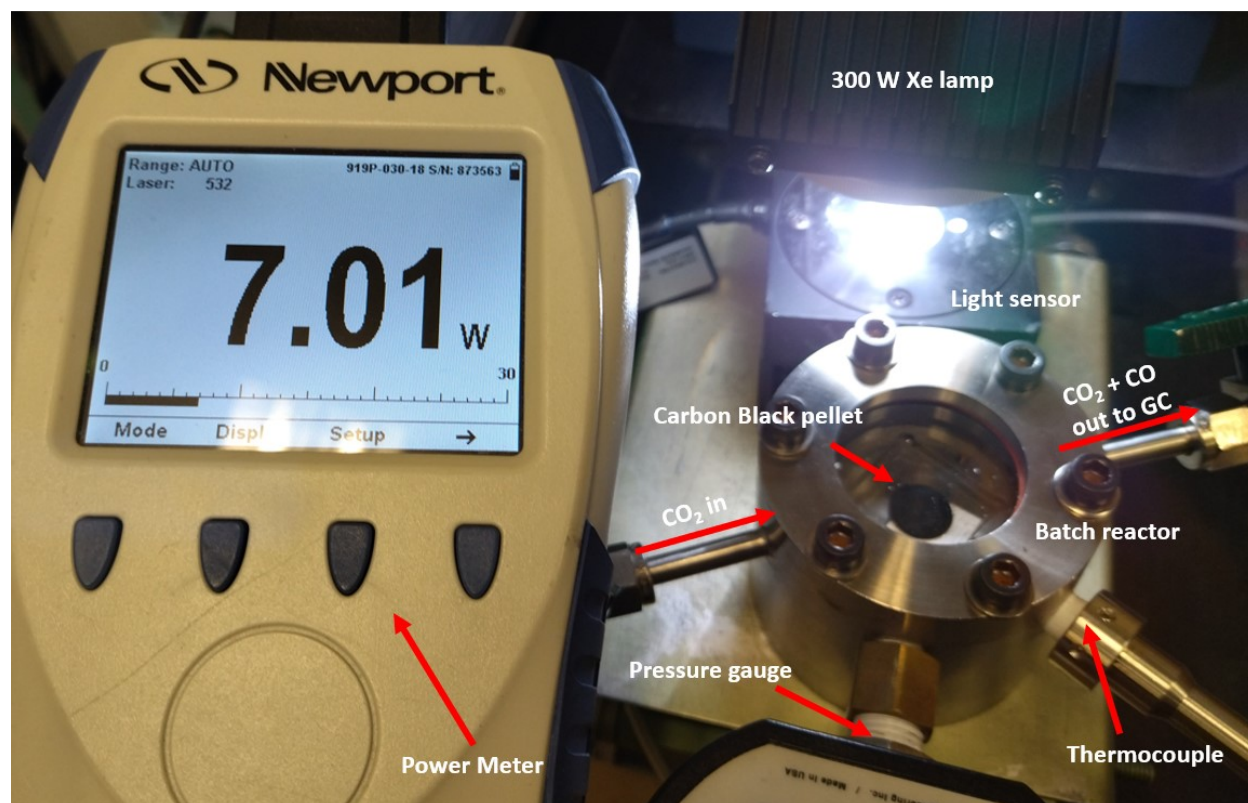
Figure S9. Setup for batch photo Boudouard process using a Perfect Light solar simulator 300W Xe lamp. The reactor had a volume of 11.8 mL and utilized a quartz window, temperature thermocouple and pressure gauge. A Newport power meter with an 18 mm detector spot diameter was used. By manually varying the power (current between 10 to 20 amp) in the Xe lamp (from 7.00 W to 27.05 W) and the diameter of the light spot (6 to 10 mm using focusing lenses), we could reach net light intensities from 12.7 W cm^{-2} to 34.4 W cm^{-2} used in this study and presented in Fig. 2.

For the solar tests, the spot diameter of irradiation was 2 mm, and the unfocused natural light intensity was 2.85 W for a maximum focused light irradiation of ~ 90 W cm^{-2} (**Fig. 3a**).

Section S10. Calculation details for the surface reaction pathway

Spin-polarized density functional theory (DFT) calculations were performed using the Vienna Ab-initio Simulation Package (VASP)[2,3] on a 128-atom, 4-layer graphite(0001) surface (constructed from cif file of ref. [4] via the Crystallography Open Database[5]) with at least 15 Å of vacuum in the c direction (see Figure S10a below). For all calculations, we used the Strongly Constrained and Appropriately Normed (SCAN) functional by Perdew *et. al*.[6] combined with the rVV10 van der Waals correction[7] implemented within VASP[8], a 600 eV energy cutoff, and a Brillouin zone sampling at the Γ point only due to the size of the unit cell. Structural relaxation was performed with the top 2 layers of the unit cell allowed to relax and the bottom 2 fixed until the norms of all forces within the unit cell are < 0.03 eV/Å The projected augmented wave (PAW) formalism was adopted for the pseudopotentials, with the GW version of the pseudopotentials used for all elements.
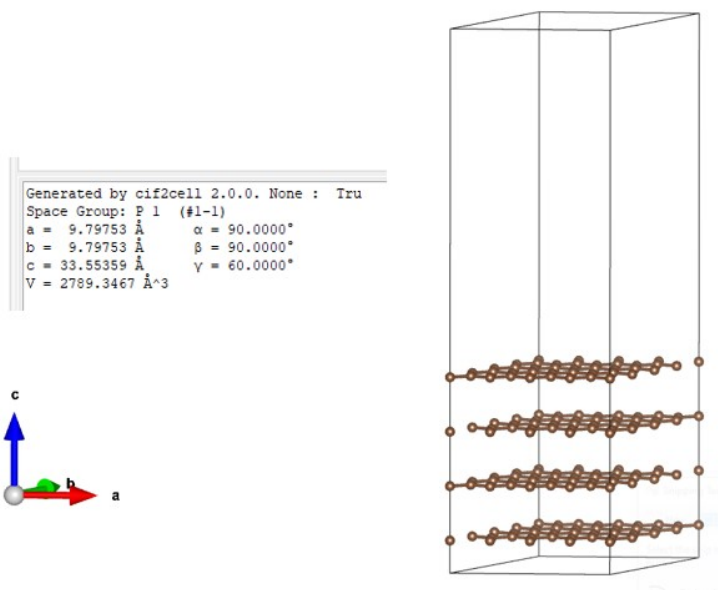


```
Generated by cif2cell 2.0.0. None :  Tru
Space Group: P 1  (#1-1)
a =  9.79753 Å      α = 90.0000°
b =  9.79753 Å      β = 90.0000°
c = 33.55359 Å      γ = 60.0000°
V = 2789.3467 Å^3
```

Figure S10a. An illustration of the graphite(0001) unit cell used for the DFT calculations.

In addition to the pristine graphite surface, five different models of surface defects (created near the centre of the unit cell) were attempted (Figure S10b):

a. Simply removing one surface carbon atom (C46)
b. Removing one surface carbon atom (C46) and capping the dangling bonds (4 unfilled valences) with four hydrogen atoms
c. Removing one surface carbon atom (C46) and capping the dangling bonds with a surface ketone and two hydrogen atoms
d. Removing one surface carbon atom (C46) and capping the dangling bonds with a surface hydroxide and two hydrogen atoms
e. Replacing one surface carbon atom (C46) with an oxygen

The ability of each surface to adsorb CO_2 was first tested by placing a bent CO_2 molecule near the defect site (or in the case of the pristine graphite, near the center of the unit cell) and allowing the structure to relax fully. Upon relaxation, only models a, d, and e had CO_2 adsorption intact (Figure S10c), and as a result, only they were used for subsequent modelling of reaction intermediates involving CO formation and a subsequent surface reaction with a second CO_2 molecule (Figure S10d). Placing the CO_2 molecule directly on the surface without bending does not result in adsorption. However, placing the bent configuration results in the stable configurations as noted above – this observation indicates that there is likely a large kinetic barrier towards the CO_2 adsorption step that could be

facilitated photochemically. Kinetic and photochemical studies on the reaction pathways between each intermediate are beyond the scope of this report and will be presented in a future publication.

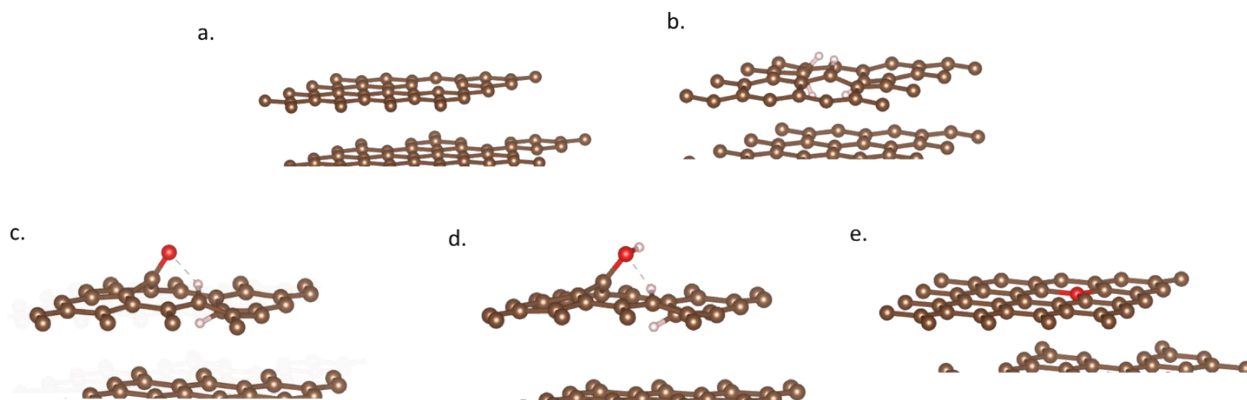**Figure S10b.** Five different models were employed for surface defects. a) ideal graphitic layers, b) 1-C vacancy c) 1-C vacancy, replaced by ketone C=O and added 2H capped d) 1-C vacancy, replaced by an -OH and added 2H capped e) 1-C substitution by a -O-.
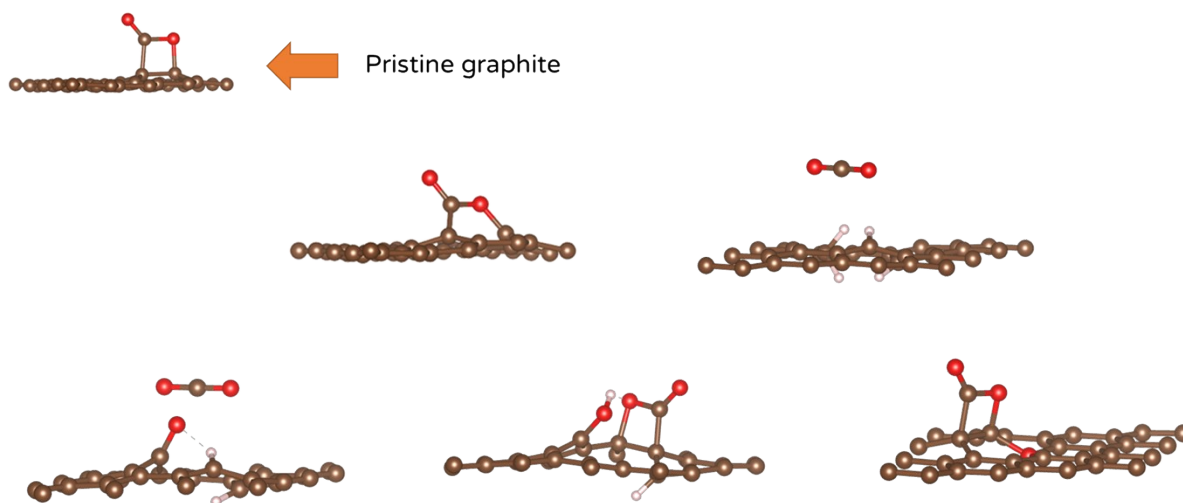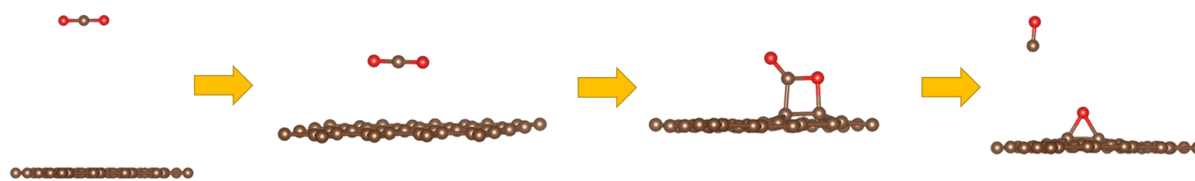

Pristine graphite

Figure S10c. Results of CO_2 adsorption tests on pristine graphite and the five surface defect models, main coordination mode $\eta^2 O, C$ [9]

1st CO$_2$ adsorption

2nd CO$_2$ adsorption
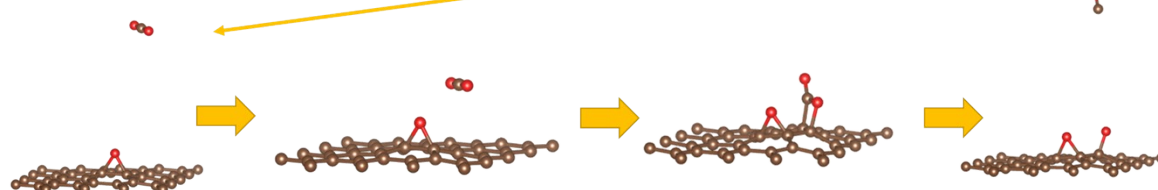
Figure S10d. The surface reaction sequence and intermediates involved for CO$_2$ adsorption on the carbon surface model (the pristine graphite surface is used here for illustration purposes).

Within the surface periodic boundary model we employed, which does not allow the loss of graphitic carbon atoms from surface edges, losing a graphitic carbon directly out of a surface lattice site as part of CO formation was not energetically favourable (Fig. S10e). Given experimental observations on an equal amount of ^{12}C and ^{13}C produced in the reaction, we believe that such processes are much more likely to occur at edge sites that could not be captured due to limitations with our model. However, the favourable effect of surface oxygenated species as intermediates of the reaction and potential agents that facilitate the process is consistent with experimental observations.

Coordinates of each structure are available in VASP POSCAR format, along with a table of the energies corresponding to Figure S10e, which can be found in Supplementary File 1.

Figure S10e. Energetic landscape of the intermediates involved in two consecutive CO_2 adsorption and CO formation steps on the graphite(0001) surface model and its defected variants a, d, and e, as shown in Figure S10b.
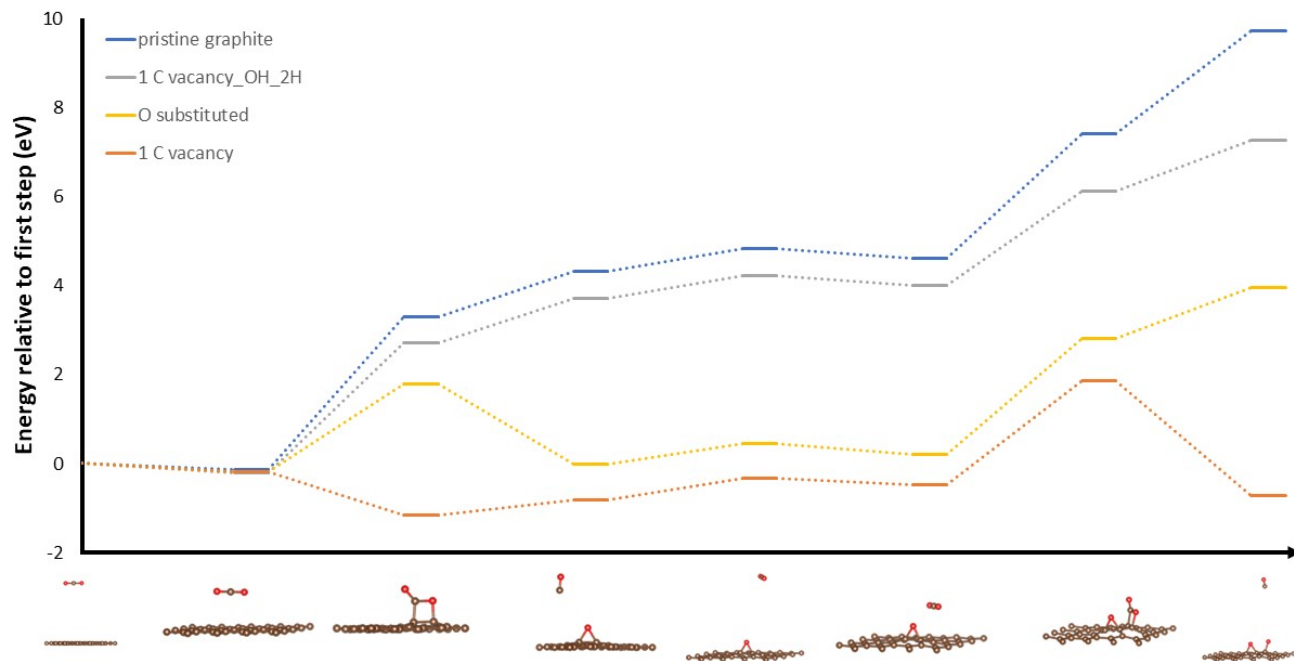
Material S11. Mathematical model for process systems analysis

Indexes are presented as lower-case italicized roman characters, sets and subsets as upper-case bold roman characters, parameters as italicized Greek characters, and variables as upper-case italicized roman characters. Super-indexes are used exclusively for notation purposes; they are written using capital, non-bold, non-italicized roman characters.

Sets

$i \in I$	Unit operations present in the flowsheet
I^C	Parabolic collector units
I^{COMP}	Compressors used in storage units
I^{ST}	Storage tanks
I^M	Mixer units
I^R	Reactor units
I^S	Separation units
I^P	Splitter units
$j \in J$	Streams
J^{FD}	Feedstock streams
J^{SR}	Feed streams for make-up solvents
J^{IN}_i	Inlet stream to unit i
J^{OUT}_i	Outlet stream from unit i
$k \in K$	Components
K^{REF}_r	Reference component in reaction r
$r \in R$	Reactions
$t \in T$	Time periods (years) in which the project is divided

Variables

NPV	Net present value
$C^{CAPITAL}$	Capital investment
$C^{WORKING}$	Working capital
$C^{FEEDSTOCK}$	Total costs of feedstocks
$C^{UTILITIES}$	Total utilities cost
C^{FIXED}	Fixed costs
$C^{CAPITALINV}_i$	Installed cost of unit operation i
E^{GEN}	Total electricity generated using by-products
E_i	Rate of electricity consumption in unit operation i
$E^{BATTERY}$	Batteries storage capacity
E^{LED}_i	Rate of electricity demand in by the LED system
F^{MASS}_j	Mass flow of stream j
F^{MOL}_j	Molar flow of stream j
$F^{MOL}_{j,k}$	Molar flow of component k in stream j
$F^{REF}_{r,i}$	Reference component in reaction r occurring in unit i
$F^{REACTOR}$	Mass flow entering each of the N reactors modules
H_j	Enthalpy of stream j
N	Total number of reactors
Q^C_i	Cold utility consumption in unit i
Q^H_i	Hot utility consumption in unit i
Q^{RF}_i	Refrigeration utility consumption in unit i
$S^{REVENUE}$	Total revenues
$S^{CREDITS}$	Total credits received from by-products
$S^{SALVAGE}$	Salvage value at the end of the project
$S^{DEPRECIATION}$	Depreciation
SF_j	Split fraction toward stream j
TCI_i	Total capital investment for unit i

Z	Minimum selling price

Parameters

α	Plant capacity in terms of the total amount of CO produced
$\beta^{C\_REF}_i$	Reference capital cost used to estimate the total capital investment of unit i
$\beta^{FM\_REF}_i$	Reference mass flow used to estimate capital and operating cost of unit i
β^{SE}	Total amount total amount of energy in the form of light that reaches the reactor.
$\beta^{MOISTURE}$	Moisture content in the carbonaceous material entering the reactor
β^{ASH}	Ash content in the carbonaceous material entering the reactor
γ_i	Factor used to oversize units in intermittent operation
δ^{LN}	Duration of the longest night
δ^{LED}	Cost of the LED system as a fraction of the reactor cost
$\eta_{r,k}$	Selectivity toward component k in reaction r
$\varepsilon_{j,k}$	Fraction of component k directed toward stream j in a separation unit
$\theta^{PERFORMANCE}_t$	Factor that determines the performance of the biorefinery in period year t
θ^E	Cost of electricity from the grid
θ^H	Cost of hot utilities
θ^C	Cost of cold utilities
θ^{RF}	Cost of refrigeration
θ^{FEED}_j	Cost of feedstock stream j
θ^{TAX}	Government tax rate
$\theta^{DEPRECIATION}_t$	Depreciation factor used in time period t
θ^{RATE}	Internal rate of return
θ^{TCI}	Factor used to determine the total capital investment for a piece of equipment
λ^{MW}_k	Molecular weight of component k
λ^{HF}_k	Enthalpy of formation of component k
λ^{CP}_k	Heat capacity of component k
λ^{LHV}_k	Low heating value of component k
$\lambda^{CO_2|C}$	$CO_2|C$ fraction in the reactor inlet
λ^{ASH}	Maximum ash content in the reactor inlet
ϕ^T_j	Temperature of stream j
ϕ^{REF}	Reference temperature
ϕ^{SR}	Rate of solvent replacement in sorption processes
δ	Conversion
η^{BRE}	Roundtrip battery efficiency
η^{PCE}	Power conversion efficiency
η^{SCE}	Light to chemical efficiency
η^{CHE}	Chemical to electricity conversion efficiency

Equations

In both processes, the equations used in the model are mostly the same (differences will be indicated by adding the letter "e" to the equations exclusively used to model the LED-P case and the letter "I" for those exclusively used to model the IO-P case). The objective function to be minimized is the minimum selling price of CO, defined as the product price that makes zero the net present value. Eqs. (1)–(10) are used to define the objective function and associated variables.

$$NPV = 0 = S^{REVENUE} + S^{CREDITS} + S^{SALVAGE} + S^{DEPRECIATION} - C^{CAPITAL} - C^{WORKING} - C^{FEEDSTOCK} - C^{UTIL}$$

$$S^{REVENUE} = ZF^{MASS}_{CO}\sum_{t \in T}\theta^{PERFORMANCE}_t\frac{\left(1 - \theta^{TAX}\right)}{\left(1 + \theta^{RATE}\right)^{t-3}} \tag{2}$$

$$S^{CREDITS} = E^{GEN}\sum_{t \in T}\theta^E\theta^{PERFORMANCE}_t\frac{\left(1 - \theta^{TAX}\right)}{\left(1 + \theta^{RATE}\right)^{t-3}} \tag{3}$$

$$S^{SALVAGE} = \left(0.35C^{CAPITAL} + C^{WORKING}\right)\frac{1}{\left(1 + \theta^{RATE}\right)^{|T|-3}} \tag{4}$$

$$S^{DEPRECIATION} = C^{CAPITAL}\sum_{t \in T}\theta^{DEPRECIATION}_t\frac{\theta^{TAX}}{\left(1 + \theta^{RATE}\right)^{t-3}} \tag{5}$$

$$C^{CAPITAL} = \sum_{i \in I}\theta^{TCI}C^{CAPITALINV}_i \tag{6}$$

$$C^{WORKING} = 0.05C^{CAPITAL} \tag{7}$$

$$C^{FEEDSTOCK} = \sum_{t \in T}\sum_{j \in J^{FD}}\theta^{PERFORMANCE}_t\theta^{FEED}_j F^{MASS}_j\frac{\left(1 - \theta^{TAX}\right)}{\left(1 + \theta^{RATE}\right)^{t-3}} \tag{8}$$

$$C^{UTILITIES} = \sum_{t \in T}\sum_{i \in I}\theta^{PERFORMANCE}_t\left(\theta^E E_i + \theta^H Q^H_i + \theta^C Q^C_i + \theta^{RF} Q^{RF}_i\right)\frac{\left(1 - \theta^{TAX}\right)}{\left(1 + \theta^{RATE}\right)^{t-3}} \tag{9}$$

$$C^{FIXED} = \sum_{t \in T}0.025C^{CAPITAL}\frac{\left(1 - \theta^{TAX}\right)}{\left(1 + \theta^{RATE}\right)^{t-3}} \tag{10}$$

We use the following general definitions: the total molar flow of each stream (Eq. 11), the total mass flow (Eq. 12), and the stream enthalpy (Eq. 13).

$$F^{MOL}_j = \sum_{k \in K}F^{MOL}_{j,k}, \forall j \in J \tag{11}$$

$$F^{MASS}_j = \sum_{k \in K}\lambda^{MW}_k F^{MOL}_{j,k}, \forall j \in J \tag{12}$$

$$H_j = \sum_{k \in K}\left(\lambda^{HF}_k + \lambda^{CP}_k\left(\phi^T_j - \phi^{REF}\right)\right)F^{MOL}_{j,k}, \forall j \in \left(J^{IN}_i \vee J^{OUT}_i\right), i \in I \tag{13}$$

We include mass balances for four types of process units: (1) mixing and storage units (Eq. 14) (2) reactors (Eq. 15), (3) separation units (Eq. 17), and (4) splitters (Eq. 18). Importantly, the set I^{ST} representing the storage units is empty in the LED-P case. We note that the mass balance for separation units is written in terms of parameter $\varepsilon_{j,k}$, which denotes the fraction of component k that is sent to stream j by the separation unit. Since this is an exploratory study, we have assumed that perfect separations occur (i.e., $\varepsilon_{j,k} = 0$ or $\varepsilon_{j,k} = 1$).

$$\sum_{j \in J^{IN}_i}F^{MOL}_{j,k} = \sum_{j \in J^{OUT}_i}F^{MOL}_{j,k}, \forall k \in K, i \in \left(I^{ST} \cup I^M\right) \tag{14}$$

$$\sum_{j \in J^{IN}_i}F^{MOL}_{j,k} + \sum_{r \in R}\delta\eta_{k,r}F^{REF}_r = \sum_{j \in J^{OUT}_i}F^{MOL}_{j,k}, \forall k \in K, i \in I^R \tag{15}$$

$$F^{REF}_{r,i} = \sum_{k \in K^{REF}_r}\sum_{j \in J^{IN}_i}F^{MOL}_{j,k}, \forall r \in R, i \in I^R \tag{16}$$

$$F^{MOL}_{j,k} = \varepsilon_{j,k}\sum_{j' \in J^{IN}_i}F^{MOL}_{j,k}, \forall k \in K, j \in J^{OUT}_i, i \in I^S \tag{17}$$

$$F^{MOL}_{j,k} = SF_j\sum_{j' \in J^{IN}_i}F^{MOL}_{j,k}, \forall k \in K, j \in J^{OUT}_i, i \in I^P \tag{18}$$

$$\sum_{j \in J^{OUT}_i}SF_j = 1, \forall i \in I^P \tag{19}$$

The capital costs for the different process units was calculated in Eqs. (20)–(26). In this work, we assumed that the photocatalytic reactors are designed modularly (Eqs. 20–22); such that their capital cost increases linearly with the number of modular reactors required. Both in the LED-P and in the IO-P, the total number of reactors needed was calculated as the ratio between the change of enthalpy in the reaction and the total amount of energy incorporated in the products (Eq. 21). This amount of energy is determined as the product between the light to chemical efficiency (η^{SCE}) and the total amount of (β^{SE}) energy in the form of light that reaches the reactor. The value of β^{SE} has been established based on the work by Kim and coworkers.[10,11] We assumed that this value is the same for both the LED-P and the IO-P. In the IO-P case we estimate the cost of the parabolic solar collectors required (Eq. 23l). We note that Eq. 20 contains a factor δ^{LED}, this factor accounts for the cost of installing and LED system. In the IO-P case it is equal to zero, while in the LED-P case it has been set equal to 1. In general, it is difficult to find information about the capital cost of photocatalytic reactors; as a first approximation, it is reasonable to assume that the cost of the LED system is as expensive as the reactor itself. The cost of separation operations and the cost of the compressors required in the IO-P case are estimated in Eq. 24. Again, we note that the set of compressors I^{COMP} is empty in the LED-P case. Finally, in Eq. 25 we calculate the storage tanks' cost. This value is scaled with respect

to the maximum amount of mass stored ($\delta^{LN}F^{MASS}_j$, where δ^{LN} is the duration of the longest night estimated based on historical data).[12]

$$TCI_i = (1 + \delta^{LED})\beta^{C\_REF}_i \gamma_i N \left(\frac{F^{REACTOR}}{\beta^{FM\_REF}_i}\right)^{0.67}, \forall i \in I^R \tag{20}$$

$$N = \frac{\sum_{j \in J^{OUT}_i} H_j - \sum_{j \in J^{IN}_i} H_j}{\beta^{SE}\eta^{SCE}} \tag{21}$$

$$F^{REACTOR} = \frac{\sum_{j \in J^{IN}_i} F^{MASS}_j}{N} \tag{22}$$

$$TCI_i = \lambda^{C\_REF}_i \gamma_i N, \forall i \in I^C \tag{23I}$$

$$TCI_i = \beta^{C\_REF}_i \left(\frac{\gamma_i F^{MASS}_j}{\beta^{FM\_REF}_i}\right)^{0.67}, \forall i \in (I^S \cup I^{COMP}) \tag{24}$$

$$TCI_i = \beta^{C\_REF}_i \left(\frac{\delta^{LN} F^{MASS}_j}{\beta^{FM\_REF}_i}\right)^{0.67}, \forall i \in (I^{ST}) \tag{25I}$$

In the LED-P, the capital cost associated with the battery system is estimated using Eq. 26, while the capacity of the battery system using Eq. 27. We note that we assume that the process remains operational in the longest night, and the batteries are sized accordingly.

$$TCI_i = \beta^{C\_REF}_i \left(\frac{E^{BATTERY}}{\beta^{E\_REF}_i}\right)^{0.67}, \forall i \in I^S \tag{26e}$$

$$E^{BATTERY} = \frac{\delta^{LN}}{\eta^{PCE}\eta^{SCE}\eta^{BRE}} \left(\sum_{j \in J^{OUT}_i} H_j - \sum_{j \in J^{IN}_i} H_j\right), \forall i \in I^R \tag{27e}$$

The utilities consumption is estimated based on the assumed duration of an average day (10 hours) by using Eqs. (28)-(32).

$$E_i = \beta^{E\_REF}_i \sum_{j \in J^{IN}_i} \frac{F^{MASS}_j}{\beta^{FM\_REF}_i}, \forall \in (I^S \cup I^{ST} \cup I^{COMP}) \tag{28}$$

$$Q^H_i = \beta^{QH\_REF}_i \sum_{j \in J^{IN}_i} \frac{F^{MASS}_j}{\beta^{FM\_REF}_i}, \forall i \in (I^S \cup I^{ST} \cup I^R) \tag{29}$$

$$Q^C_i = \beta^{QC\_REF}_i \sum_{j \in J^{IN}_i} \frac{F^{MASS}_j}{\beta^{FM\_REF}_i}, \forall i \in (I^S \cup I^{ST} \cup I^R) \tag{30}$$

$$Q^{RF}_i = \beta^{QRF\_REF}_i \sum_{j \in J^{IN}_i} \frac{F^{MASS}_j}{\beta^{FM\_REF}_i}, \forall i \in (I^S \cup I^{ST} \cup I^R) \tag{31}$$

The electricity demand in the LED system used in the LED-P case is calculated in Eq. 32. This equation assumes that the electricity is obtained directly from photovoltaics for 10 hours (average day), and the remaining time (at night=14 hours) comes from the battery system.

$$E^{LED}_i = \left(\frac{(10/24)}{\eta^{PCE}\eta^{SCE}} + \frac{(14/24)}{\eta^{PCE}\eta^{SCE}\eta^{BRE}}\right)\left(\sum_{j \in J^{OUT}_i} H_j - \sum_{j \in J^{IN}_i} H_j\right), \forall i \in I^R \tag{32e}$$

The electricity generated from the by-products is estimated in Eq. 33.

$$E^{GEN} = \sum_{k \in K} \eta^{EFF}\lambda^{LHV}_k F^{MOL}_{j,k}, \forall j \in J^E \tag{33}$$

The plant capacity is constrained to a fixed value Eq. 34.

$$F^{MASS}_j = \alpha, \forall j \in J^{FD} \tag{34}$$

Additionally, we impose constraints on the fraction of CO_2:C (Eq. 35) and ash content (Eq. 36) at the reactor entrance.

$$\sum_{j \in J^{IN}_i} F^{MOL}_{j,CO_2} = \lambda^{C|CO_2}\left(\sum_{j \in J^{IN}_i} F^{MOL}_{j,C} + \sum_{j \in J^{IN}_i} F^{MOL}_{j,BIOCHAR}\right), \forall i \in I^R \tag{35}$$

$$\sum_{j \in J_i^{IN}} F_{j,k} = \lambda^{ASH}\left(\sum_{j \in J_i^{IN}} F_{j,C}^{MOL} + \sum_{j \in J_i^{IN}} F_{j,BIOCHAR}^{MOL}\right), \forall i \in I^R \qquad (36)$$

We also define equations to set the composition of the original carbon source. The parameters used in these equations are defined based on experimental data. Two components are considered: moisture (Eq. 38) and ashes (Eq. 39).

$$\lambda_{WATER}^{MW} F_{BIOCHAR,WATER}^{MOL} = \beta^{MOISTURE} F_{BIOCHAR}^{MASS} \qquad (37)$$

$$\lambda_{ASH}^{MW} F_{BIOCHAR,ASH}^{MOL} = \beta^{ASH} F_{BIOCHAR}^{MASS} \qquad (38)$$

Finally, we calculate the amount of sorbent that is necessary to replace (Eq. 40) in separation operations.

$$F_j^{MASS} = \phi^{SR} \sum_{j' \in J_{CO\_SEPARATION}^{IN}} F_{j'}^{MASS}, \forall j \in J^{SR} \qquad (39)$$

Material S12 Reference values for capital and operating costs

The economic parameters used in the model are summarized in table S12-1.

Table S12-1. Values for the parameters used in the model

Equipment	λ^{FR}	λ^{CC} [MM\$]	λ^{QH} [MJ/s]	λ^{QC} [MJ/s]	λ^{QR} [MJ/s]	λ^{E} [MJ/s]	ϕ^{T} [°C]	γ^{LED}	γ^{I}	Ref.
Crushing and drying	71.367 Kg/s	25.516	0.065			0.62		1	2	13,14
Reactor	0.0027 Kg/s	0.001 (0.002)*					30	1	2	15
Hydrocyclone	142.37 Kg/s	2.14				0.059		1	2	Aspen
Storage reaction products	78.73 Kg/s	77.3		10.39		14.74			1	Aspen
CO₂ Storage	77.63 Kg/s	11.2		7.06		5.99			1	Aspen
CO capture	7.65 Kg/s	8.840	5.13			2.82		1	1	16
CO₂ capture	75.594 Kg/s	47.547	3.77		39.6	7.17		1	1	Aspen
Collector		0.025							2	15
Batteries	5.76x10¹⁰ Kg/s	8.440						1		17

*The base case for the reactor, in parenthesis, corresponds to the LED system, we assume a more expensive reactor in this case.[15] For the intermittent refinery, we assume that the reactor design will be simpler than in the LED case and we assume that the cost of the reactor is half of the LED case.

In tables S12-2 and S12-3 we show the separation factors used to model the LED-P and IO-P. Note that for simplicity, we assume perfect separations.

Table S12-2. Values for $\varepsilon_{j,k}$ in the LED-P

Streams		Coal	Ash	CO₂	CO	CH₄	H₂	C	W
Origin	Destination								
Solid separation	Splitter1	1	1					1	
Solid separation	CO₂ capture			1	1	1	1		
CO₂ capture	Splitter2			1					
CO₂ capture	CO capture				1	1	1		
CO capture	Main product				1				
CO capture	Byproducts					1	1		
Crushing and drying	Mixer	1	1						
Crushing and drying	Waste treatment								1

Table S12-3. Values for $\varepsilon_{j,k}$ in the IO-P

Streams		Coal	Ash	CO₂	CO	CH₄	H₂	C	W
Origin	Destination								
Solid separation	Splitter1	1	1					1	
Solid separation	Gas storage			1	1	1	1		
CO₂ capture	Splitter2			1					
CO₂ capture	CO capture				1	1	1		
CO capture	Main product				1				
CO capture	Byproducts					1	1		
Crush and drying	Mixer	1	1						
Crush and drying	Waste treatment								1

The relevant physical properties for the different components are shown in table S12-4.

Table S12-4 Relevant physical properties for the components in the model

	λ_k^{MW} [Kg/mol]	λ_k^{HF} [J/mol]	λ_k^{CP} [J/mol-K]	λ_k^{LHV} [J/mol]
Coal	0.01389	0	0.019	-437484
Ash	0.01474	0	0.019	0
CO2	0.044	-393510	45.719	0
CO	0.028	-110530	30.341	-277828
CH4	0.016	-74520	50.206	-800640
H2	0.002	0	29.301	-233920
C	0.012	0	20.813	-1020000
W	0.01802	-241818	36.02	0

The value for the economic and performance parameters in the model is shown in **Table S12-5**. The capacity has been fixed such that the plant can process approximately the same amount of CO_2 produced by the NREL refinery.[18] Battery efficiency was set at 85% based on the current state of the art.[19] Likewise, the collector efficiency has been determined based on an NREL report for solar parabolic collector systems.[20] The power conversion efficiency was established conservatively, considering that at similar wavelength, efficiency can be ~81% operating under optimal conditions. Since the process's operation conditions may not be optimal, we have used a lower estimate of 60% [21]. The light to chemical efficiency is directly related to the quantum yield is difficult to determine, especially because specialized reactors may improve its value. We have conservatively assumed a value of 30%, this would yield an overall solar to chemical efficiency of 22.5 for the IO-P case, which is not unreasonable and is inline with assumptions from previous studies.[15]

Table S12-5. Value for economic and performance parameters used in the model

Parameter	Symbol	Value	Units
Thermodynamic reference temperature	ϕ^{REF}	25	°C
Maximum ash content in the reactor inlet	λ^{ASH}	10	%
$CO_2|C$ fraction in the reactor inlet	$\lambda^{C|CO_2}$	3	-
Plant capacity	α	130	Mol-CO/s
Rate of solvent replacement in sorption processes	ϕ^{SR}	0.08	-
Roundtrip battery efficiency	η^{BRE}	85	%
Power conversion efficiency	η^{PCE}	60	%
Collector efficiency	η^{C}	75	%
Light to chemical efficiency	η^{SCE}	30	%
Chemical to electricity conversion efficiency	η^{CHE}	40	%
Factor to determine the total capital investment	θ^{TCI}	2.55	[-]
Sorbent cost	$\theta_{SORBENT}^{FEED}$	0.8	$/Kg
CO_2 cost	θ_{CO2}^{FEED}	39	$/Ton
Biochar cost	$\theta_{BIOCHAR}^{FEED}$	350	$/Ton
Cost of electricity from the grid	θ^{E}	1.59e-8	$/J
Cost of hot utilities	θ^{H}	2.32e-9	$/J
Cost of cold utilities	θ^{C}	1.9e-10	$/J
Cost of refrigeration	θ^{RF}	2.54e-9	$/J

For the performance rate, we used the same assumptions of the NREL lignocellulosic ethanol plant, such that in the first three years, there is no production. Thus the performance factor is zero, the fourth year operation is 75%, and every year afterwards has 100% efficiency.[22] For the depreciation rate, we use MACRS method.[23]

Material S13. Sensitivity Analysis
To further understand the impact of the parameters on the MSP, we present in **Figure S13-1** and **Figure S13-2** heat maps with a sensitivity analysis. The figures explore how changes in the chemistry, operation, feedstock cost, and capital cost parameters impact the MSP. In the chemistry category, conversion plays the more relevant role in the IO-P, while the light to chemical efficiency (η^{SCE}) is more critical in the LED-P (**Figure S13-1a** - **Figure S13-2a**). This result is expected; higher conversions are associated with lower gas storage requirements, which are a major cost driver in the IO-P. On the other hand, a higher η^{SCE} implies lower electricity consumption and, therefore, lower needs for battery storage, which are major cost drivers in LED-P. From the operational parameters (**Figures 4b-5b**), we have two insights: first, increasing the amount of ash that can be present at the reactor inlet does reduce the MSP; however, the improvements that can be gained from changing this factor diminish as more ash is allowed in the reactor feed. $\lambda^{CO_2|C}$ has a significant impact in both processes, reducing $\lambda^{CO_2|C}$ impacts both the feedstock requirements and equipment size. The effect of changing the cost of feedstocks (CO_2 and biochar) is studied in **Figure S13-1c** - **Figure S13-2c**. In the figures, the cost of CO_2 can take values as low as US\$ 0 mt^{-1}, which reflects possible subsidies for carbon capture that may lower the final CO_2 cost. The figures show that

carbon cost has a more pronounced effect than the cost of CO_2. One observation from **Figure S13-1c** is that there is a slope change when the price of CO_2 is US\$ ~15 mt^{-1}. This change of slope is related to a change in process configuration. When the price of CO_2 is below US\$ ~15 mt^{-1} there is no economic incentive to store it overnight. In other words, the recycle stream and the CO_2 storage unit are not used anymore in the process design. Finally, **Figures S13-1d – S13-2d** show the effect of changing the capital costs; we break these costs into two parameters: the reactor system (includes collector and reactor in the intermittent operation), and the separations. The results in this plot are presented such that the axes can be read as fractional increases/savings on the capital costs.
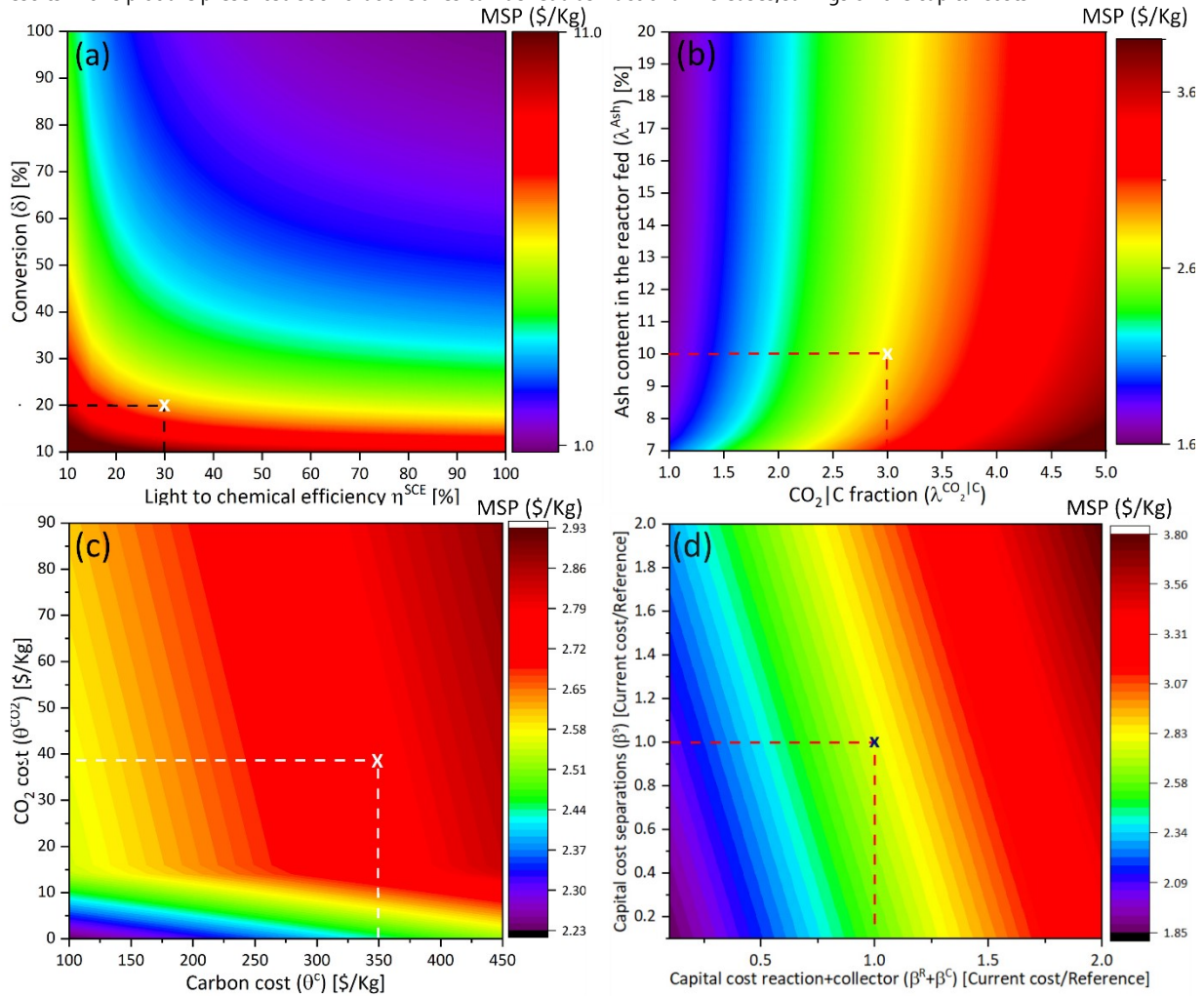
Figure S13-1. Sensitivity analysis of MSP in the IO-P to parameters in the following categories (a) Chemistry (b) Operation (c) Feedstock cost (d) Capital cost. The reference value based on the base case scenario is shown with an "X".
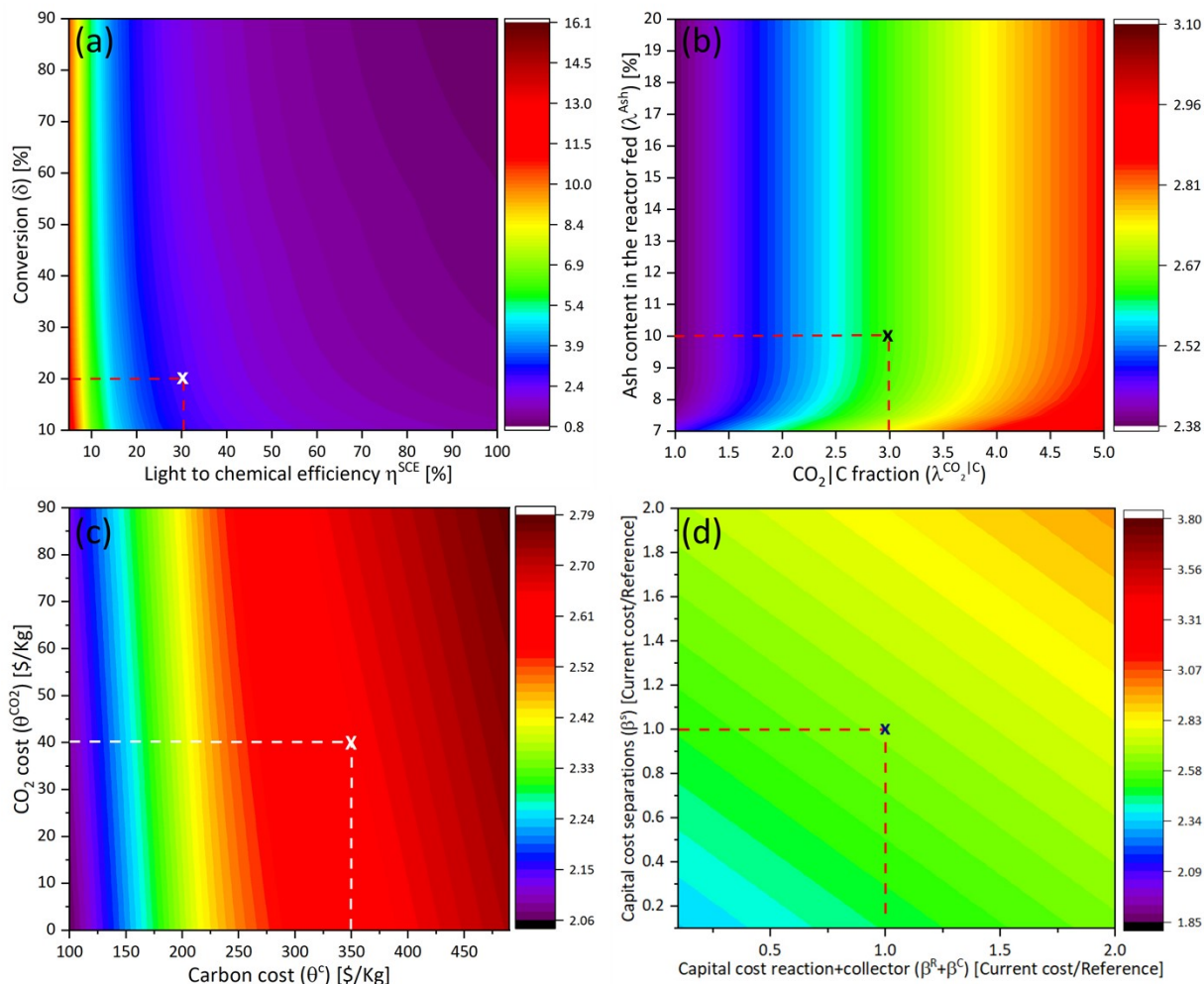
Figure S13-2. Sensitivity analysis of MSP in the LED-P to parameters in the following categories (a) Chemistry (b) operation (c) Feedstock cost (d) Capital cost. The reference value based on the base case scenario is shown with an "*X*".

Figure S13-3, presents a sensitivity analysis for the variables exclusively related to the LED operation. **Figure S3a** explores the effect of changing the battery cost (y-axis) and the LED efficiency (x-axis). **Figure S3b** shows the battery system parameters: costs and roundtrip efficiency. Both parameters have a significant effect on process economics, but the effect of roundtrip efficiency is less pronounced. We note that based on USDOE goals and projections, battery cost could be as low as US$ 88 kWh[-1] by 2050 and battery efficiency as high as 95%.[24,25]
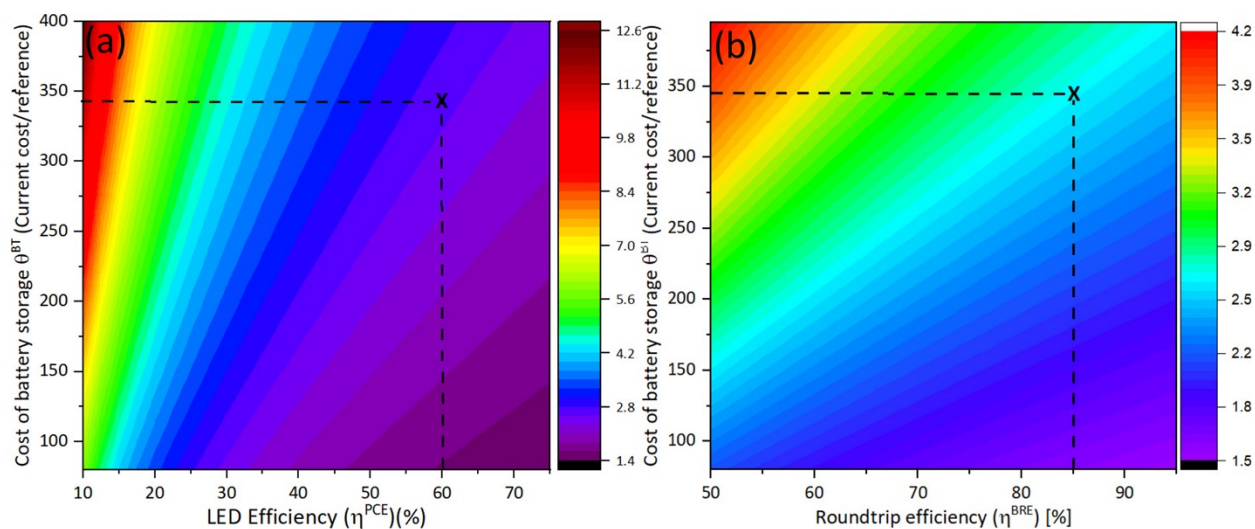
Figure S13-3. Sensitivity analysis of the MSP in the LED-P concerning (a) Cost of battery storage and LED efficiency (b) Cost of battery storage and battery roundtrip efficiency. The reference value based on the base case scenario is shown with an "X".

Material S14. LED-P-a 2050 vision

In this subsection, we pose a vision for the 2050 photocatalytic process design. **Figure S14-1** shows the expected MSP when implemented incremental improvements (from left to right) in the IO-P and LED-P parameters. The improvements on these parameters have been selected based on reasonable assumptions or considering the targets for the different parameters established by the U.S. Department of Energy or other U.S. government agencies. The cost of storing electricity in batteries is expected to decrease in the coming decades significantly; we assume that the cost of storing energy will be US$ 150 kWh^{-1} by 2050.[26] This value is a conservative estimate consistent with NREL projections, we note that their more optimistic simulations US$ 88 kWh^{-1} are achieved. The battery roundtrip efficiency is projected to reach 95%, some battery systems currently available have already achieved this value, which will become more common in the future[26] In the US, the cost of renewable electricity from photovoltaics is projected to reach a value of US$ 0.02 kWh^{-1} by 2030[27] Likewise, the power conversion efficiency for LEDs is expected to rise to 86%;[28] we have selected a more conservative estimate of 70% in our projections.

Regarding the feedstocks, we estimate that biochar cost will be available at US$ 150 mt^{-1}, a significant improvement in comparison with the current cost. For CO_2, we assume that the 2050 target of US$ 30 mt^{-1} will be achieved.[29] We assume that significant reductions in the reactor system will be achieved (~50%); this assumption is made by considering that photocatalytic reactors are still under development and can significantly improve. On the other hand, separations, a more mature technology, are not expected to improve significantly, and we assume only 20% savings. For operational conditions, we assume that the ash content in the reactor could be increased to 15%, and the $CO_2|C$ fraction reduced to 2. Finally, we assume that improvements in the reaction conditions will increase the conversion and solar to chemical efficiency to 30% and 60%, respectively. The main conclusion drawn from the plot is that the intermittent and LED technologies are not significantly different from each other in terms of the MSP achievable in the medium and long term. The operational advantages of LED-P make them an attractive option. However, the economic viability of these systems is contingent upon the development of efficient and low-cost battery storage systems, photovoltaic conversion systems, and LEDs.
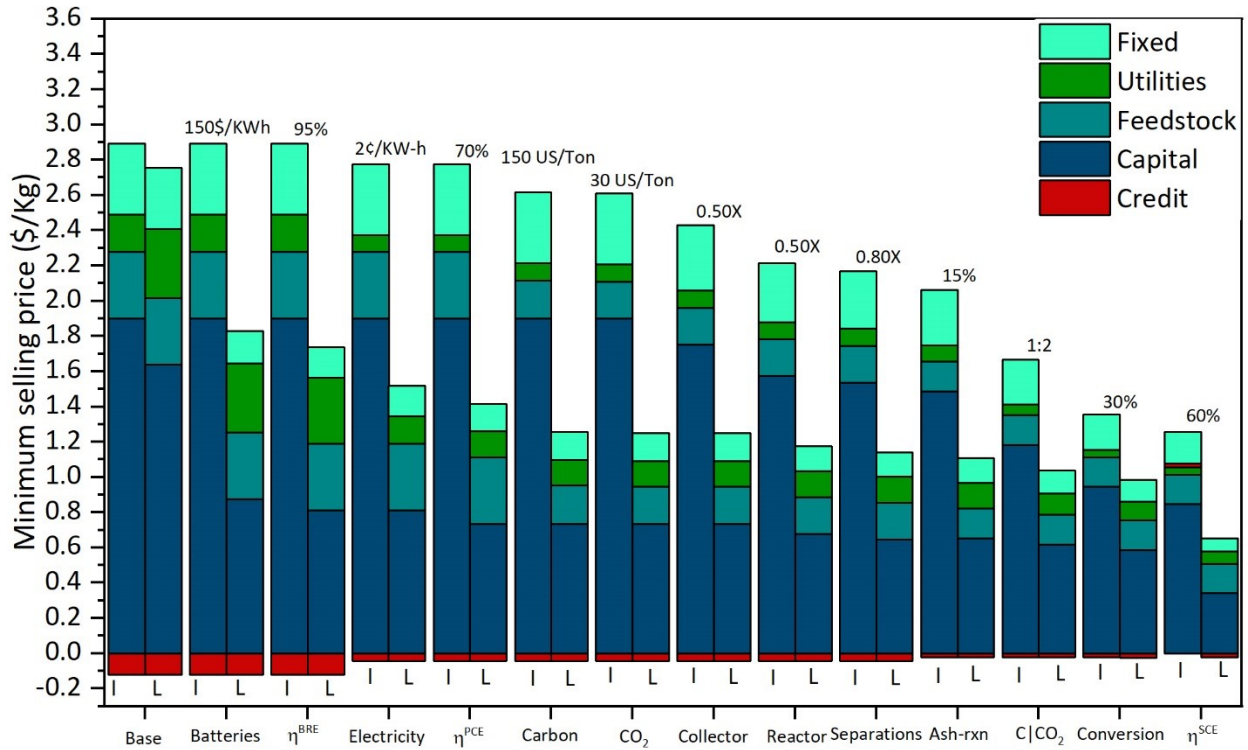
Figure S14-1. c. The value on top of the columns represents the new value used in the simulation and it can be compared with the reference case in **Table S1**.

Material S15. Estimated cost for syngas

In **Figure S15-1**, we show the MSP of synthesis gas as a function of the CO content ($MSP_{Syngas} = \lambda MSP_{CO} + (1 - \lambda)MSP_{H_2}$). We assume that the Boudouard reaction produces CO and the hydrogen is produced by water gas shift reaction (WGS) to estimate this price. The cost associated with the WGS process is calculated based on a detailed Aspen plus simulation. The financial parameters used to calculate the MSP of hydrogen were identical to those used in NREL ethanol production biorefineries.[18] The plant designed to perform the water gas shift reaction is shown in **Figure S15-2**. It consists of a reactor where the WGS reaction occurs, followed by a flash tank where unconverted water is condensed. The kinetics of the reaction is modelled using data from Hla *et al.* 2009.[30] The conversion in the reactor is almost complete. After the reaction system, we used a compression and separation system, this system allows us to obtain a hydrogen-rich stream (92%) and a CO_2-rich stream.
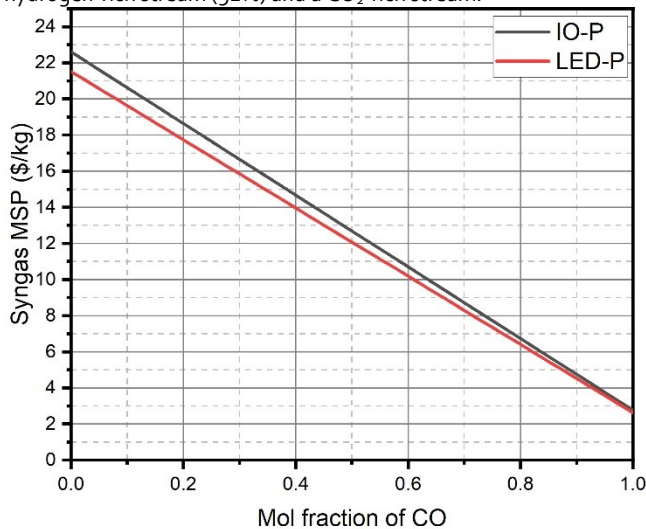

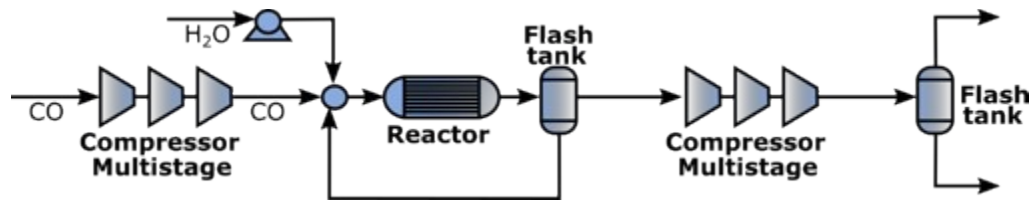**Figure S15-1. Synthesis gas cost as a function of CO mol fraction**

Figure S15-2. A plant used to produce hydrogen using the water gas shift reaction

Material S16. Life cycle assessment

We perform a cradle-to-gate life cycle analysis of the LED-P and IO-P processes using the GaBi software and the associated energy database. The analysis assumes that biochar production has an inventory of emissions similar to those reported by Hamedani and coworkers.[31] In our calculations, we did not account for CO_2 credits associated with biochar application to soil, provided that we are using it to produce chemicals. We assumed that CO_2 was captured from the fermentation outlet in an ethanol production plant. The energy requirements associated with CO_2 capture are determined based on the work of Geisler and Maravelias.[32] The functional unit selected is kg-CO and the only environmental category analyzed is global warming potential. Following a displaced burden strategy, we distribute the environmental burden between main products and co-products (electricity).

Figure S16-1 shows the GHG emissions for the IO-P and the LED-P in four different scenarios. Those labelled as Initial correspond to scenarios based on the base case design, while those labelled as optimized correspond to the most optimistic outcome in **Figure S14**. In each case, we explore the possibility of supplying utilities using fossil fuels or alternatively using solar energy. In all cases, negative emissions are obtained, and the LED-P case displays a significantly better performance.
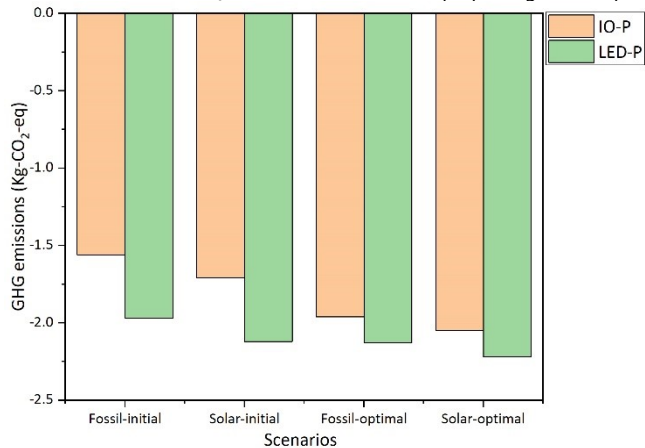

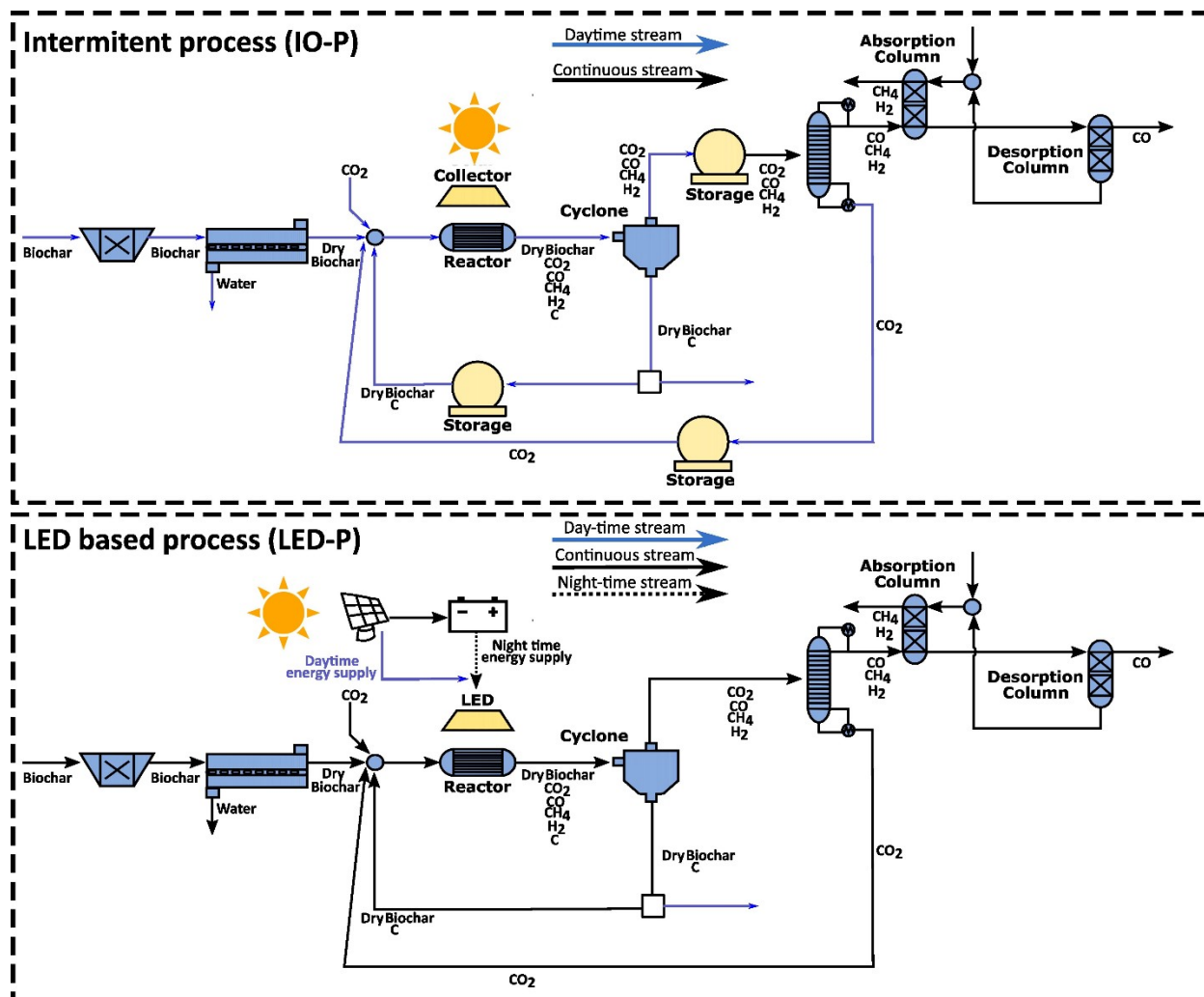**Figure S16.1.** GHG emissions estimated for the cradle-to-gate Boudouard processes

Figure S17. Flow diagram of biorefineries operating intermittently using solar energy (IO-P) or using LEDs (LED-P). Note that some streams (blue) operate intermittently in the IO-P system. In the LED-P process a battery system is used to supply electricity during night time to the LEDs in the photocatalytic reactor.

Supplementary references

1   G. A. Zickler, B. Smarsly, N. Gierlinger, H. Peterlik and O. Paris, *Carbon*, 2006, **44**, 3239–3246.

2   G. Kresse and J. Furthmüller, *Computational Materials Science*, 1996, **6**, 15–50.

3   G. Kresse and J. Furthmüller, *Physical Review B*, 1996, **54**, 11169–11186.

4   P. Trucano and R. Chen, *Nature 1975 258:5531*, 1975, **258**, 136–137.

5   S. Gražulis, D. Chateigner, R. T. Downs, A. F. T. Yokochi, M. Quirós, L. Lutterotti, E. Manakova, J. Butkus, P. Moeck and A. Le Bail, *Journal of Applied Crystallography*, 2009, **42**, 726–729.

6   J. Sun, A. Ruzsinszky and J. Perdew, *Physical Review Letters*, 2015, **115**, 036402.

7   H. Peng, Z. H. Yang, J. P. Perdew and J. Sun, *Physical Review X*, 2016, **6**, 041005.

8   J. Klimeš, D. R. Bowler and A. Michaelides, *Physical Review B - Condensed Matter and Materials Physics*, 2011, **83**, 195131.

9   M. Aresta, A. Dibenedetto and E. Quaranta, *Reaction mechanisms in carbon dioxide conversion*, 2015.

10   J. Kim, J. E. Miller, C. T. Maravelias and E. B. Stechel, *Applied Energy*, 2013, **111**, 1089–1098.

11   J. Kim, C. A. Henao, T. A. Johnson, D. E. Dedrick, J. E. Miller, E. B. Stechel and C. T. Maravelias, *Energy & Environmental Science*, 2011, **4**, 3122.

12   X. Peng, T. W. Root and C. T. Maravelias, *AIChE Journal*, 2019, **65**, 10–16.

13   DOE/NETL, *Technical Report*, 2010, 442.

14   S. V. Jangam, M. Karthikeyan and A. S. Mujumdar, *Drying Technology*, 2011, **29**, 395–407.

15   J. Kim, C. A. Henao, T. A. Johnson, D. E. Dedrick, J. E. Miller, E. B. Stechel and C. T. Maravelias, *Energy Environ Sci*, 2011, **4**, 3122.

16   Y. Il Lim, J. Choi, H. M. Moon and G. H. Kim, *Korean Chemical Engineering Research*, 2016, **54**, 320–331.

17   T. Aquino, M. Roling, C. Baker and L. Rowland, *Battery Energy Storage Technology Assessment Platte River Power Authority*, 2017.

18   D. Humbird, R. Davis, L. Tao, C. Kinchin, D. Hsu, A. Aden, P. Schoen, J. Lukas, B. Olthof, M. Worley, D. Sexton and D. Dudgeon, *Process Design and Economics for Biochemical Conversion of Lignocellulosic Biomass to Ethanol: Dilute-Acid Pretreatment and Enzymatic Hydrolysis of Corn Stover*, Golden, CO (United States), Colorado, 2011.

19   EIA, Utility-scale batteries and pumped storage return about 80% of the electricity they store.

20   C. Kutscher, F. Burkholder and J. Kathleen Stynes, *Journal of Solar Energy Engineering, Transactions of the ASME*, , DOI:10.1115/1.4005247.

21   P. Kusuma, P. M. Pattison and B. Bugbee, *Horticulture Research*, , DOI:10.1038/s41438-020-0283-7.

22   D. Humbird, R. Davis, L. Tao, C. Kinchin, D. Hsu, A. Aden, P. Schoen, J. Lukas, B. Olthof, M. Worley, D. Sexton and D. Dudgeon, *Process Design and Economics for Biochemical Conversion of Lignocellulosic Biomass to Ethanol: Dilute-Acid Pretreatment and Enzymatic Hydrolysis of Corn Stover*, Golden, CO (United States), Colorado, 2011.

23   M. M. El-Halwagi, *Sustainable Design Through Process Integration*, Elsevier, 2012.

24   EIA, Utility-scale batteries and pumped storage return about 80% of the electricity they store.

25   W. Cole, A. W. Frazier, W. Cole and A. W. Frazier, *Cost Projections for Utility-Scale Battery Storage : 2020 Update*, 2020.

26   W. Cole, A. W. Frazier, W. Cole and A. W. Frazier, *Cost Projections for Utility-Scale Battery Storage : 2020 Update*, 2020.

27   U.S. Department of Energy, *The SunShot 2030*, 2017.

28   P. Morgan Pattison, M. Hansen and J. Y. Tsao, *Comptes Rendus Physique*, 2018, **19**, 134–145.

29   C. Cunliff, *Federal Energy R&D: Carbon capture*, 2019.

30   S. S. Hla, D. Park, G. J. Duffy, J. H. Edwards, D. G. Roberts, A. Ilyushechkin, L. D. Morpeth and T. Nguyen, *Chemical Engineering Journal*, 2009, **146**, 148–154.

31   S. R. Hamedani, T. Kuppens, R. Malina, E. Bocci, A. Colantoni and M. Villarini, *Energies*, 2019, **12**, 1–21.

32   C. H. Geissler and C. T. Maravelias, *Applied Energy*, 2021, **302**, 117539.